ACS Energy LETTERS

http://pubs.acs.org/journal/aelccp

Electrochemical Production of >1 M Acid and Base from Neutral Salt at High Current Density and Low Energy Demand

J. Gage Wright and Matthew W. Kanan*

Cite This: *ACS Energy Lett.* 2025, 10, 5328−5335

Read Online

ACCESS | Metrics & More | Article Recommendations | Supporting Information

ABSTRACT: Consumption of acid and base drives chemical transformations underpinning industrial hydrometallurgical processes and many proposed carbon management technologies. Production of acid and base is the key driver of the energy demand, emissions, and waste generation of these processes. Generating acid and base electrochemically from salt solutions enables their production without stoichiometric waste using low-carbon power. However, conventional electrochemical approaches using ion-exchange membranes (IEMs) have an excessive energy demand, low productive current densities, and poor impurity tolerance. These shortcomings can be addressed by the diaphragm flow cell (DFC), which has a lower resistance and an improved impurity tolerance. Here we report an improved DFC design that produces a concentrated (1.1−1.5 M) acid and base from neutral salt at the lowest energy demand (0.051−0.067 kWh mol^{-1}) and highest productive current densities (275−367 mA cm^{-2}) reported to date at 70 °C, a realistic temperature for a scaled system. Using a continuum model, we show that the electrolyte residence time has a significant impact on current efficiency by controlling diffusive losses.

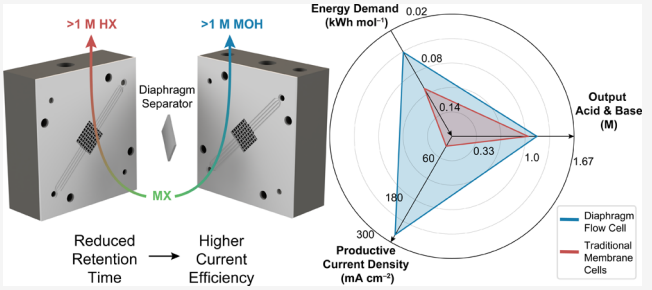

Acids and bases are widely used in industrial processes to extract and purify chemicals and materials. For example, Ni and Co hydroxide precipitates that are feedstocks for stainless steel and Li ion battery cathodes are obtained from limonite ores by sequential acidic leaching and basic precipitation.[1,2] Rare earth elements are separated from each other using hundreds of solvent extraction stages wherein acid and base are consumed in the transfer of rare earth ions from one phase to another.[3] Battery recycling technologies that are being scaled up to handle growing volumes of end-of-life batteries also utilize multiple acid−base steps to extract Li and transition metal ions from spent cathodes.[4,5] The (super)-stoichiometric consumption of acid and base in such processes comes with a significant energy cost and emissions footprint, and generates large volumes of salt waste products, which are becoming increasingly problematic.[6]

The dominant acid and base used at scale are H_2SO_4 and $Ca(OH)_2$ (slaked lime). H_2SO_4 is produced by oxidation and hydration of elemental sulfur generated by petroleum desulfurization, and $Ca(OH)_2$ is made by hydrating CaO, which is produced by calcination of $CaCO_3$. Because $CaCO_3$ calcination is highly endothermic ($\Delta H°$ = 178 kJ mol^{-1}), $Ca(OH)_2$ production uses 0.031−0.065 kWh of thermal energy per mol of base equivalent for calcination alone, which is supplied by coal or natural gas combustion.[7] Beyond H_2SO_4 and $Ca(OH)_2$, HCl and NaOH are also widely utilized. NaOH is a direct product of the chlor-alkali process, whereas most HCl is produced as a byproduct of hydrocarbon chlorination processes, which utilize the Cl_2 generated by chlor-alkali.[8] As such, NaOH and HCl have the embedded energy cost of chlor-alkali, which corresponds to 0.088 kWh per one mole of acid and base.[9]

As an alternative to conventional sources, acid and base can be generated from salt solutions by using electrochemistry to drive the dissociation of water into H^+ and OH^- and the selective transport of salt ions into separate streams. Electrochemical acid−base production is attractive because it can readily be powered by low-carbon energy and it eliminates salt waste by turning acid and base into regenerable reagents.[10] It also has potential applications for carbon management, for which waste production is completely infeasible. To this end,

Received: July 24, 2025
Revised: September 13, 2025
Accepted: September 22, 2025

https://doi.org/10.1021/acsenergylett.5c02318
ACS Energy Lett. 2025, 10, 5328−5335

recent studies have described lab-scale processes that use electrochemically generated acid and base to concentrate CO_2 from air[11−15] and seawater,[16−18] or to produce reactive solids for CO_2 mineralization[19,20] and building materials.[21−24]

The fundamental challenges for current methods of electrochemical acid−base production are energy demand and throughput. The commercial technology is bipolar membrane electrodialysis (BPMED), which consists of a repeating cell that has three solution compartments, a bipolar membrane (BPM), an anion exchange membrane (AEM), and a cation exchange membrane (CEM) (Figure S1A). Application of a voltage drives water dissociation at the BPM to produce H^+ in the acid compartment and OH^- in the base compartment while cations migrate from the salt compartment across the CEM to balance the OH^- and anions migrate across the AEM to balance the H^+. BPMED can generate concentrated (>1 M) and relatively pure acid and base solutions, but the use of three compartments and multiple ion exchange membranes (IEMs) per cell imposes large resistive losses that result in a high energy demand per mol of acid and base generated (E_{ab}) and low current density (j).

The thermodynamic minimum energy required to generate 1 M H^+ and OH^- solutions from a salt solution input is 0.022 kWh mol^{-1} (see Note S1). To generate ≥1 M acid and base with a BPMED system, E_{ab} ranges from 0.073 to 0.21 kWh mol^{-1} with a productive current density (j_{prod}, the total current density (j_{tot}) minus recombination losses) less than 40 mA cm^{-2}.[25−27] In addition, BPMED cannot tolerate polyvalent cations that are likely to be present in a closed-loop process (e.g., Ca^{2+}, Mg^{2+}, Ni^{2+}) because precipitation of polyvalent metal hydroxides in the ion channels of CEMs causes permanent damage to this component.[28−30]

Recent advances in fabrication[31−33] and water dissociation catalysis[34,35] have improved the performance of the BPM component of BPMED. However, as shown independently in two recent reports,[36,37] the cell voltage (E_{cell}) quickly becomes dominated by resistive losses across the IEMs for j_{tot} > ∼60 mA cm^{-2} in cells configured to generate acid and base. The AEMs used in BPMED are especially resistive because they are designed to block crossover of highly mobile H^+ ions.[38,39] Although there has not been a thorough investigation of the efficiency of a BPMED system that uses advanced BPMs to date, these results indicate that improving the BPM does not address the root cause of efficiency loss.

To address the limitations of BPMED and other IEM-based acid/base generation technologies, we previously reported the design of a diaphragm flow cell (DFC) for acid−base generation (Figure 1A).[40] The DFC minimizes resistive losses by using only two compartments and replacing IEMs with a single diaphragm spacer, which has pores that are much larger in diameter (ca. 100 nm) than the ion channels of IEMs. To minimize E_{cell}, we used the H_2 oxidation reaction (HOR) and H_2 evolution reaction (HER) for electrochemical H^+ and OH^- generation, respectively. Recombination of H^+ and OH^- is suppressed by using a high electrolyte concentration such that transport of electrolyte ions (M^+, X^-) out-competes H^+/OH^- transport. This design outputs acid and base solutions containing additional electrolyte, but the presence of salt is inconsequential for many closed-loop applications. We showed that the DFC could produce acid and base at lower E_{ab} and higher j_{prod} than BPMED systems and demonstrated that the output solutions could be used in closed-loop processes that extract $Mg(OH)_2$ from ultramafic rocks. We also showed that

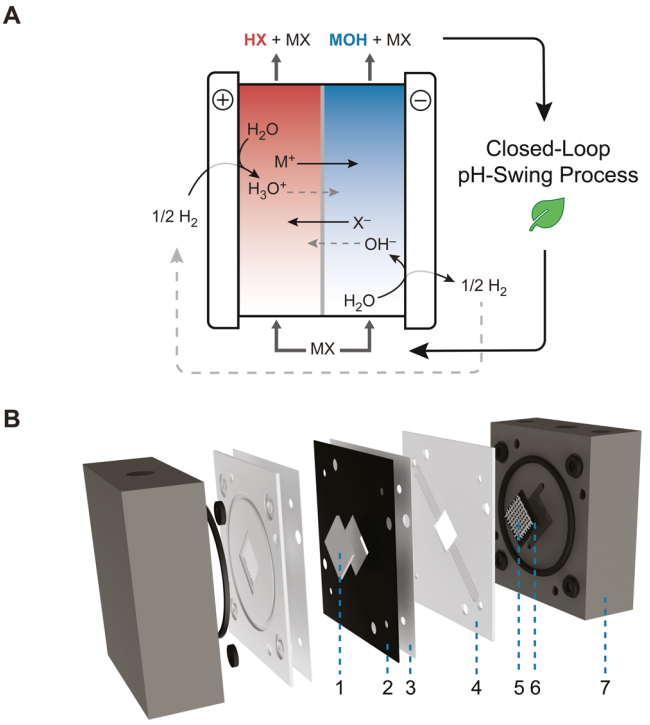

Figure 1. (A) Diagram of the DFC generating acid and base in a closed-loop hydrometallurgical process. (B) Expanded render of the 1 cm^2 cell used in this work. It is composed of (1) Zirfon Diaphragm Separator, (2) Framing Gasket, (3) Face Gaskets, (4) Flow Plates, (5) Spacers, (6) Gas Diffusion Electrodes, and (7) Cell Hardware.

the cell design can be stacked by using a bipolar gas diffusion electrode (Figure S1B), although it should be noted that the cell design is also stackable with suitably stable BPMs, which could potentially reduce losses from kinetic overpotentials.

Here we report engineering advances that substantially improve the performance of the DFC. We show that rigidifying the electrolyte compartments and reducing the electrolyte residence time increases current efficiency (CE), defined as the yield of acid and base per electron, thereby reducing E_{ab} while increasing j_{prod}. We also investigate the temperature dependence of acid−base production and find that performance increases at moderately elevated temperatures that are relevant for real devices. Using an input of KCl electrolyte and optimized conditions, the DFC can generate 1.1−1.5 M HCl and KOH solutions at 70 °C with E_{ab} = 0.051−0.067 kWh mol^{-1} and j_{prod} = 275−367 mA cm^{-2}, which to our knowledge is the most efficient and high-throughput acid−base generation reported to date.

The DFC has a symmetrical cell design consisting of two flow plates with electrolyte compartments separated by a Zirfon diaphragm (Figure 1B). The compartments are contacted by gas diffusion electrodes (GDEs) that are coated with catalysts for HOR and HER. The back sides of the GDEs are contacted with Ti cell blocks. In our previous study of the DFC, the electrolyte compartments had no internal support structures. For this work, we inserted plastic woven mesh spacers into the electrolyte compartments to provide rigidity in the current-carrying direction and reduce the residence time by reducing the compartment volume. Mesh spacers are a common design feature for membrane-based electrodialyzers.[41]

https://doi.org/10.1021/acsenergylett.5c02318
ACS Energy Lett. 2025, 10, 5328−5335

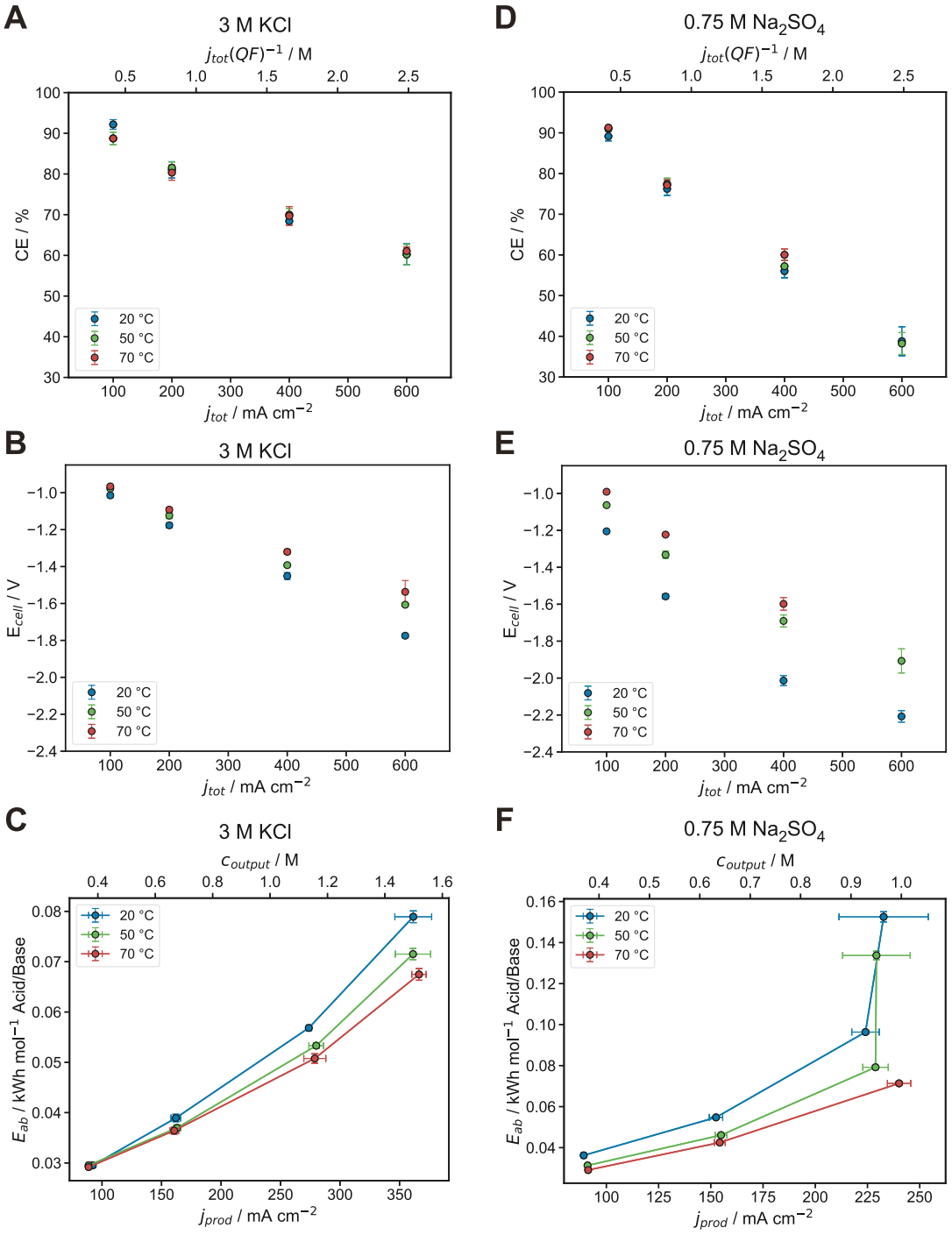

Figure 2. Efficiency data for different temperatures as a function of current density as electrolyte is flowed through each compartment at Q = 0.15 mL min^{-1} cm^{-2}. (A) Current efficiencies and (B) cell potentials for 3 M KCl versus total current density.(C) Energy required per mole to generate the acid and base streams for 3 M KCl versus productive current density. (D) Current efficiencies and (E) cell potentials for 0.75 M Na_2SO_4 versus total current density. (F) Energy required per mole to generate the acid and base streams for 0.75 M Na_2SO_4 versus productive current density. Error bars represent the standard deviation of at least 3 independent samples.

Acid−base production was performed by flowing electrolyte at a fixed flow rate through each compartment and supplying H_2 to the anode while applying a fixed current (see Supporting Information). H^+ and OH^- are electrogenerated by HOR at the anode and HER at the cathode, respectively. The concentration of product ions in each electrolyte stream exiting the cell (c_{output}) depends on j_{tot}, the current efficiency (CE), and the flow rate of the electrolyte normalized to the electrode surface area (Q) according to

$$c_{output} = \frac{j_{tot} \cdot CE}{QF} = \frac{j_{prod}}{QF} \quad (1)$$

where j_{prod} is the productive current density, the portion of j_{tot} that results in separated H^+ and OH^- ions, and F is Faraday's constant. The quotient j_{tot}/QF is equivalent to the output concentration at 100% CE. The actual concentrations of H^+ and OH^- in the acid (anolyte) and base (catholyte) outputs of the cell were quantified by performing potentiometric titrations

https://doi.org/10.1021/acsenergylett.5c02318
ACS Energy Lett. 2025, 10, 5328−5335

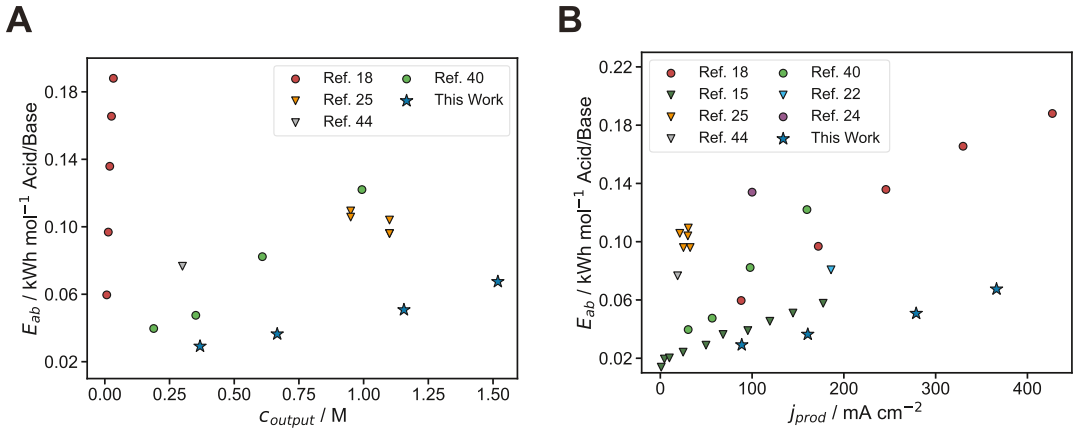

Figure 3. Comparison of E_{ab} for producing strong acid and base equivalents across the literature[44] as a function of (A) output concentration and (B) productive current density. Cells in which the acid or base is consumed in situ, for example to liberate CO_2 using electrogenerated acid, are excluded from panel A. Triangles indicate cells that are prone to fouling by polyvalent metal cations. Circles indicate cells that are not prone to fouling by polyvalent metal cations. Stars indicate the DFC in this work running with 3 M KCl at 70 °C.

of aliquots of each stream, and the measured concentrations were used to determine CE and j_{prod}. The energy demand of the cell per mol of acid and base generated is given by

$$E_{ab} = \frac{E_{cell}F}{CE} \quad (2)$$

where E_{cell} is the full cell potential.

The thermoneutral voltage for acid−base production is substantially smaller than the thermodynamic voltage (i.e., $|\Delta H°| < |\Delta G°|$). As a result, an acid−base producing cell will generate heat, even at zero overpotential (see Note S1). We estimated that the heat generated at relevant current densities would be enough to raise the operating temperature by a few tens of degrees (see Note S2), and therefore incorporated temperature control in our cell design. To operate at elevated temperatures, the cell was heated using electrically insulated heaters on either side of the Ti blocks and the electrolyte was pumped through a preheater (see Supporting Methods and Figure S2).

We first performed experiments using 3 M KCl as the input electrolyte to generate HCl and KOH. KCl was chosen over NaCl due to its higher conductivity,[42] which reduces *iR* losses, and the higher transference number for K^+ relative to Na^+, which improves CE. We collected CE and E_{cell} data for cells operating at j_{tot} values ranging from 100 − 600 mA cm^{-2} with a fixed flow rate of Q = 0.15 mL min^{-1} cm^{-2}, each at 20, 50, and 70 °C (Figure 2 and Table S1). At 20 °C, the CE was 92.2% at 100 mA cm^{-2} and remained above 60% up to 600 mA cm^{-2} (Figure 2A). These values are substantially higher than what is observed when operating without a mesh spacer (see below). Interestingly, CE was not affected by operating temperature, indicating that the high values seen at ambient temperature would be maintained in a real system operating at elevated temperature. Because the conductivity of the electrolyte increases with temperature, E_{cell} was reduced by increasing the temperature, with a 250 mV difference between 20 and 70 °C at 600 mA cm^{-2} (Figure 2B).

The key performance metrics for generating HCl and KOH from neutral 3 M KCl are summarized in Figure 2C. Remarkably, the DFC produced 1.16 M outputs at 275 mA cm^{-2} of productive current density with an energy demand of only 0.051 kWh mol^{-1} at 70 °C. The output concentrations could be increased to 1.52 M and j_{prod} to 367 mA cm^{-2} with a higher E_{ab} of 0.067 kWh mol^{-1}, or less concentrated but still useful outputs of 0.38 M could be generated with a very low E_{ab} of 0.029 kWh mol^{-1}. To assess durability, we performed a 30 h stability test with 3 M KCl at 200 mA cm^{-2} and observed a net decay rate of just 350 μV h^{-1} and no change in CE (Figure S3).

We also used the DFC to generate acid and base from Na_2SO_4, which was chosen because it is a common hydrometallurgical waste product that poses a growing problem for industries such as battery recycling. It is challenging to regenerate acid and base from Na_2SO_4 efficiently because it is not highly soluble in water at room temperature,[43] and it exhibits a high degree of ion pairing, which limit the maximum conductance achievable with Na_2SO_4 electrolytes. Experiments were performed using 0.75 M Na_2SO_4 to avoid precipitation in the cell at 20 °C. Processing Na_2SO_4 in the DFC generates bisulfate (HSO_4^-) on the acid side (pK_a = 2) instead of H_3O^+. While masking H^+ as an anionic species is beneficial for CE, this effect is offset by the lower concentration, lower mobility of Na^+ compared to K^+, and formation of low mobility, SO_4^{2-}-masking $NaSO_4^-$ ion pairs in 0.75 M Na_2SO_4 electrolyte such that the CE is somewhat lower compared to 3 M KCl (Figure 2D). The CE again showed no dependence on temperature, but elevated temperature improved performance by reducing *iR* losses. At 70 °C, the DFC generated 0.38−0.99 M $NaHSO_4$ and NaOH solutions with E_{ab} ranging from 0.029−0.071 kWh mol^{-1} at j_{prod} of 91−240 mA cm^{-2}. With 0.75 M Na_2SO_4 at 70 °C and 600 mA cm^{-2}, the anode could no longer provide a durable phase boundary preventing intrusion of H_2 bubbles into the anode compartment, so these data are not reported in Figure 2.

The performance of the DFC demonstrated here substantially exceeds that of previously reported acid−base generating systems. Figure 3 compares key metrics for reported cells that are capable of generating at least moderately concentrated (>0.3 M) acid and base outputs and/or operating at high current density (j_{prod} > 100 mA cm^{-2}) using neutral salt inputs. The DFC is uniquely capable of generating concentrated outputs (0.37−1.52 M HCl/KOH) at low energy demand (0.029−0.067 kWh mol^{-1}) and high current density (j_{prod} of 89 mA − 367 mA cm^{-2}). By comparison, a recent study of a pilot-scale BPMED stack reported generating ∼1 M HCl and NaOH from NaCl brine with a minimum E_{ab} of 0.096 kWh mol^{-1} at

https://doi.org/10.1021/acsenergylett.5c02318
ACS Energy Lett. 2025, 10, 5328−5335

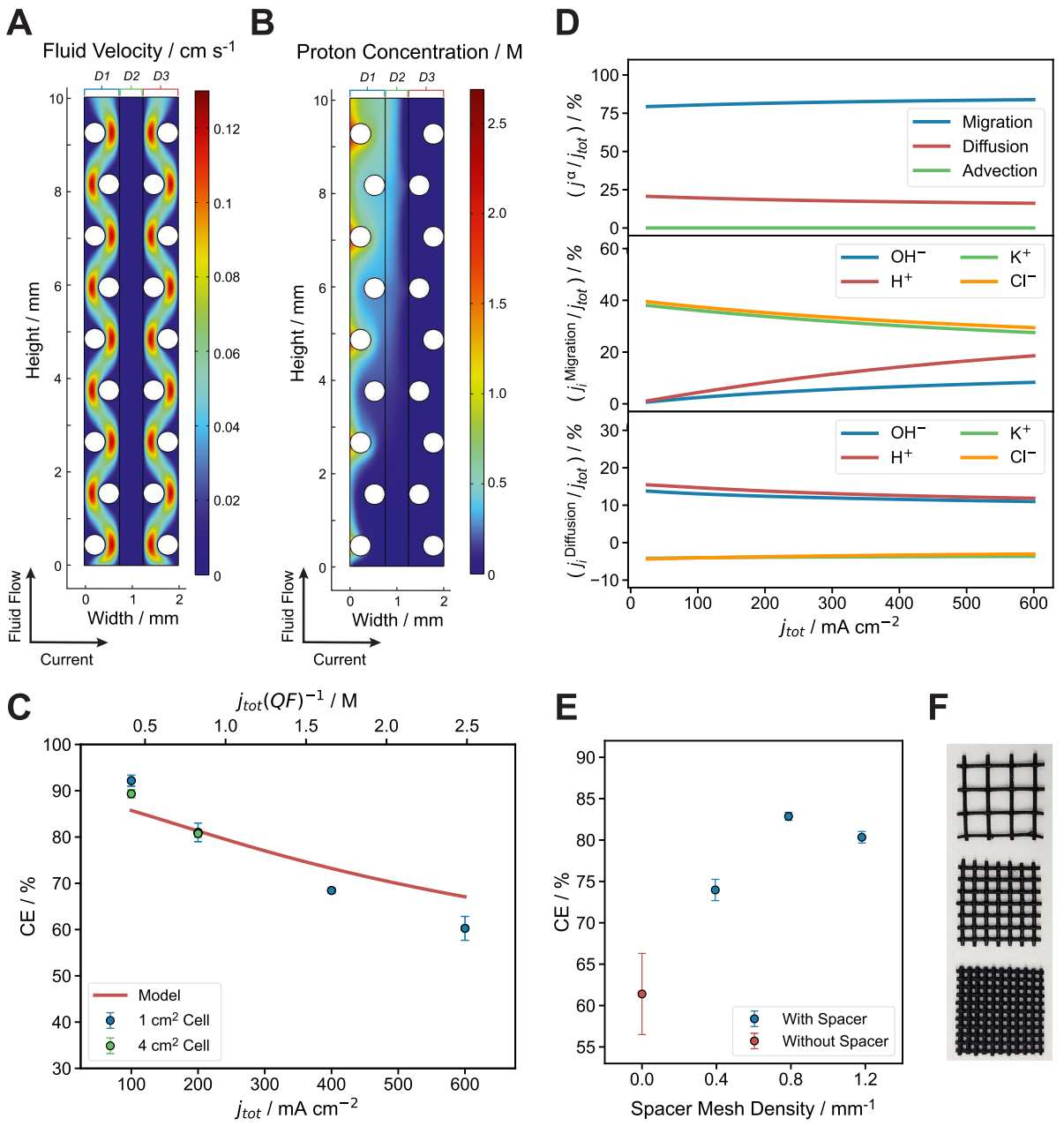

Figure 4. Predictions of the continuum model for 3 M KCl at 20 °C, 200 mA cm^{-2}, and Q = 0.15 mL min^{-1} cm^{-2} including heatmaps of (A) fluid velocity and (B) proton concentration over the simulation domain (subdomains are labeled D1: anolyte, D2: diaphragm, D3: catholyte). (C) Model predictions and current efficiency data for 3 M KCl at 20 °C and Q = 0.15 mL min^{-1} cm^{-2} collected in 1 cm^2 and 4 cm^2 cells. (D) Fractional currents carried by ion i by mechanism $\alpha(j_i^{\alpha}/j_{tot})$. (E) Current efficiency data for 3 M KCl at 20 °C, 200 mA cm^{-2}, and Q = 0.15 mL min^{-1} cm^{-2} using cells with 0.8 mm thick electrode compartments with and without spacers of varying mesh density. (F) Photograph of low, medium, and high density 3D printed spacer meshes (top to bottom). Error bars represent the standard deviation of at least 3 independent samples..

j_{prod} = 32.5 mA cm^{-2}. A recently reported acid−base generating system employing H_2 looping demonstrated high current densities (j_{prod} of 88−427 mA cm^{-2}), but only for the production of very dilute outputs (7−33 mM) and at high energy demands (E_{ab} of 0.06−0.19 kWh mol^{-1}).[18] Other studies have described cell designs that integrate electrochemical acid−base production with a chemical step performed inside the cell, such as acid-promoted decomposition of $CaCO_3$. Such integration is beneficial for CE, but comes at the expense of additional resistance and cell complexity. A recently reported acid−base generating cell with in situ $CaCO_3$ decomposition demonstrated j_{prod} = 100 mA cm^{-2}, but with large E_{ab} of 0.134 kWh mol^{-1}.

To understand the factors that determine performance of the DFC, we assembled a continuum model of the cell with physics to describe both the hydrodynamics and the discrete ion concentrations (see Supporting Information). We solved the stationary Nernst-Plank and Navier−Stokes equations on a two-dimensional representation of the cell over a wide range of current densities using the finite element method to obtain spatially resolved ion concentrations and the flux of each species from migration, diffusion, and advection. The Reynolds Number in each compartment was estimated to be <1 under

https://doi.org/10.1021/acsenergylett.5c02318
ACS Energy Lett. 2025, 10, 5328−5335

all conditions (see Note S3) and therefore laminar flow was assumed, which is in agreement with studies of the fluid dynamics in electrodialyzers with similar geometries and spacers.[45−47]

Figure 4A,B shows the fluid velocity and H_3O^+ concentration profile for one j_{tot} value (200 mA cm^{-2}) at the value of Q used for the experiments in Figure 2 (0.15 mL min^{-1} cm^{-2}). The model predicts the buildup of a large H^+/OH^- gradient from the inlet to the outlet of the anolyte/catholyte compartments. The CE for a given j_{tot} and Q was computed based on the average efflux of each species from the outlet of the anolyte and catholyte simulation domains (eq S5). Figure 4C shows the calculated CE as a function of j_{tot} at fixed Q. The model captures the trend and the CE values are in good agreement with experimental values. Notably, the CE predictions are substantially higher than what we calculated in our earlier model of the DFC, which used a fixed-point iteration method to calculate individual ion contributions to the current (Figure S4A). The fixed-point model assumes complete mixing in the electrolyte compartments, whereas the continuum model here captures spatial concentration gradients, which favor the transport of supporting electrolyte ions over H_3O^+/OH^- ions. The good agreement between experimental and modeled CE values in Figure 4C indicates that spatial gradients and thus incomplete mixing is an important factor for high CE in the DFC with mesh spacers.

The predicted value of CE depends only on the combination of operating parameters (j_{tot} and Q) and not the electrode area. To test whether the CE values were maintained at larger electrode sizes, we 3D printed a prototype 4 cm^2 cell using our rapid prototyping method[48] (Figure S5). The CE values matched those of the 1 cm^2 cell within the range of current measurable by our instruments (up to 1 A) (Figure 4C).

Figure 4D shows the relative contributions of diffusion, migration, and advection to the current as a function of j_{tot} at fixed Q. Since a finite volume of bulk electrolyte is charge balanced, the model correctly predicts that the current carried by advection is 0. The total contributions of migration and diffusion show essentially no dependence on j_{tot}. As j_{tot} is increased, the electric field experienced by the ions and the concentration of H_3O^+ and OH^- are increased, which increases migration; at the same time, there is an increase in ion concentration gradients, which increases diffusion. In terms of individual ions, the contribution of the migration of H_3O^+ increases substantially and the OH^- contribution to a lesser extent, while the K^+ and Cl^- contributions decrease. This result reflects the relative mobilities of these ions and is largely responsible for the reduction in CE.

In contrast to the result when Q is fixed, CE is predicted to increase when both j_{tot} and Q are increased proportionally (Figure S6). At fixed j_{tot}/Q, the relative contribution of migration to the total current increases as j_{tot} is increased, while the individual relative contributions of H_3O^+ and OH^- to migration remain essentially unchanged because the concentrations are the same. Gratifyingly, the measured CEs were found to increase in accordance with the predicted trend for $j_{tot}(QF)^{-1}$ = 0.83 M as j_{tot} was varied from 100 to 600 mA cm^{-2}. This result shows that the volumetric productivity of the cell can be increased without sacrificing CE.

Additionally, when compared to CE data for cells assembled without spacers, as shown in Figure S4B, CEs in those cells were found to be significantly depressed.

Finally, we sought to ascertain whether the spacer mesh acts purely to maintain the separation between the electrode and separator, or whether it significantly alters the flow of electrolyte and transport of ions. Without a spacer, a cell assembled with an identical compartment thickness (0.8 mm) showed 20% lower CE than the same cell with a spacer (Figure 4E). Only some of this loss can be recovered by increasing the compartment thickness (see Note S4 and Figure S7), suggesting that the spacer has another effect beyond enforcing a fixed separation. The presence of a spacer reduces the residence time of electrolyte in the electrolyte compartment because of the volume fraction occupied by the spacer (see Note S5). We hypothesized that this reduction in residence time increases CE because the product ions (H_3O^+ and OH^-) must travel across the thickness of the electrolyte compartment to be neutralized, and fewer product ions are able to cross over per unit volume as the residence time is decreased.

To test this hypothesis, we prepared spacer meshes of different densities of threads per millimeter at identical thickness (Figure 4F and Table S2). Because woven spacer meshes with varying densities and identical thread diameter (and therefore thickness) were not available, we 3D printed a series of spacers with woven geometry (Figure S8). One spacer with a density of 0.8 mm^{-1} was designed to be as geometrically similar as possible to the polypropylene woven spacer mesh used above. We assembled cells with normal compartment thicknesses (0.8 mm) with each of these spacers and measured the CE under the same conditions (Figure 4E). At a low mesh density of 0.4 mm^{-1}, the cell achieved a CE of 74%, increasing to 83% at 0.8 mm^{-1}, which confirms that a spacer can affect CE beyond enforcing separation and supports the effect of residence time. Interestingly, increasing the thread density to 1.2 mm^{-1} resulted in a small decrease in CE to 80%. The reversal of this trend could be caused by increased convective mixing in the current-carrying direction, which diminishes product ion concentration gradients that are critical for maximizing CE. A high mesh density will also reduce the conductance of the electrolyte compartment, increasing E_{cell}. Therefore, as a general design principle, minimum E_{ab} can be achieved with an intermediate spacer thread density.

In this study, we have introduced a modified design of the DFC that includes a woven mesh spacer to support the electrolyte compartments. This modification greatly improved CE and by extension E_{ab} for generating acid and base from both KCl and Na_2SO_4 electrolytes. Studies at different operating temperatures revealed that elevated temperatures (up to 70 °C) reduced iR losses without compromising CE, which resulted in further improvements to performance. A continuum model of the DFC with spacers that captures both the hydrodynamics and ion transport phenomena revealed that large spatial ion gradients are present at steady-state, which contributes to high CE. The spacer also serves to reduce the residence time of the electrolyte in the cell, which suppresses recombination losses. Due to its combination of high throughput, output concentration, and low energy demand without the use of IEMs, this cell represents the most efficient reported method for producing strong acid and base streams that are relevant for applications in hydrometallurgy and carbon management.

https://doi.org/10.1021/acsenergylett.5c02318
ACS Energy Lett. 2025, 10, 5328−5335

■ ASSOCIATED CONTENT

Supporting Information

The Supporting Information is available free of charge at https://pubs.acs.org/doi/10.1021/acsenergylett.5c02318.

Supporting Methods for cell assembly, electrochemical measurements, current efficiency measurements, and continuum modeling. Supporting Notes regarding salt-splitting thermodynamics, cell temperature, Reynolds number, compartment thickness, and residence time. Supporting Figures showing diagrams of salt splitting stacks, a photograph of the temperature control apparatus, stability testing data, fixed-point modeling results, CE data in a cell with no spacer, modeling results and CE data sweeping j_{tot} at fixed $j_{tot}(QF)^{-1}$, CE data as a function of compartment thickness, a render of the 4 cm^2 cell, and a photomicrograph of a 3D printed spacer mesh. Supporting Tables, including the data plotted in Figure 2, and 3D printed spacer thicknesses (PDF)

■ AUTHOR INFORMATION

Corresponding Author

Matthew W. Kanan − *Department of Chemistry, Stanford University, Stanford, California 94305, United States;* orcid.org/0000-0002-5932-6289; Email: mkanan@stanford.edu

Author

J. Gage Wright − *Department of Chemistry, Stanford University, Stanford, California 94305, United States;* orcid.org/0000-0003-3938-1202

Complete contact information is available at: https://pubs.acs.org/10.1021/acsenergylett.5c02318

Notes

The authors declare no competing financial interest.

■ ACKNOWLEDGMENTS

Support for this research was provided by MAC3 and the Stanford Woods Institute for the Environment Big Ideas for the Oceans Program, the Tides Foundation, and the Canadian Institute for Advanced Research. We thank Roger Wise for assistance in 3D printing the variable density spacers. Part of this work was performed at the Stanford Nano Shared Facilities (SNSF) RRID:SCR_023230, supported by the National Science Foundation under award ECCS-2026822.

■ REFERENCES

(1) Pandey, N.; Tripathy, S. K.; Patra, S. K.; Jha, G. Recent Progress in Hydrometallurgical Processing of Nickel Lateritic Ore. *Transactions of the Indian Institute of Metals* **2023**, *76*, 11−30.

(2) Kerfoot, D. G. E. *Ullmann's Encyclopedia of Industrial Chemistry*; John Wiley & Sons, Ltd, 2000.

(3) McNulty, T.; Hazen, N.; Park, S. Processing the Ores of Rare-Earth Elements. *MRS Bull.* **2022**, *47*, 258−266.

(4) An, L. *Recycling of Spent Lithium-Ion Batteries: Processing Methods and Environmental Impacts*; Springer International Publishing AG: Cham, 2019.

(5) Jung, J. C.-Y.; Sui, P.-C.; Zhang, J. A Review of Recycling Spent Lithium-Ion Battery Cathode Materials Using Hydrometallurgical Treatments. *Journal of Energy Storage* **2021**, *35*, 102217.

(6) Müller, H. *Ullmann's Encyclopedia of Industrial Chemistry*; John Wiley & Sons, Ltd, 2000.

(7) Kenny, M.; Oates, T. *Ullmann's Encyclopedia of Industrial Chemistry*; John Wiley & Sons, Ltd, 2007.

(8) Austin, S.; Glowacki, A. *Ullmann's Encyclopedia of Industrial Chemistry*; John Wiley & Sons, Ltd, 2000.

(9) Kumar, A.; Du, F.; Lienhard, J. H. V. Caustic Soda Production, Energy Efficiency, and Electrolyzers. *ACS Energy Lett.* **2021**, *6*, 3563−3566.

(10) Binnemans, K.; Jones, P. T. The Twelve Principles of Circular Hydrometallurgy. *J. Sustain. Metall.* **2023**, *9*, 1−25.

(11) Keith, D. W.; Holmes, G.; St. Angelo, D.; Heidel, K. A Process for Capturing CO2 from the Atmosphere. *Joule* **2018**, *2*, 1573−1594.

(12) Sabatino, F.; Mehta, M.; Grimm, A.; Gazzani, M.; Gallucci, F.; Kramer, G. J.; van Sint Annaland, M. Evaluation of a Direct Air Capture Process Combining Wet Scrubbing and Bipolar Membrane Electrodialysis. *Ind. Eng. Chem. Res.* **2020**, *59*, 7007−7020.

(13) Jin, S.; Wu, M.; Jing, Y.; Gordon, R. G.; Aziz, M. J. Low Energy Carbon Capture via Electrochemically Induced pH Swing with Electrochemical Rebalancing. *Nat. Commun.* **2022**, *13*, 2140.

(14) Xi, D.; Yang, Z.; Emanuel, M. S.; Zhao, P.; Aziz, M. J. Electrochemical Acid−Base Generators for Decoupled Carbon Management. *Energy Environ. Sci.* **2025**, *18*, 3839−3851.

(15) Zhang, X.; Fang, Z.; Zhu, P.; Xia, Y.; Wang, H. Electrochemical Regeneration of High- Purity CO2 from (Bi)Carbonates in a Porous Solid Electrolyte Reactor for Efficient Carbon Capture. *Nat. Energy* **2025**, *10*, 55−65.

(16) De Lannoy, C.-F.; Eisaman, M. D.; Jose, A.; Karnitz, S. D.; DeVaul, R. W.; Hannun, K.; Rivest, J. L. Indirect Ocean Capture of Atmospheric CO2: Part I. Prototype of a Negative Emissions Technology. *International Journal of Greenhouse Gas Control* **2018**, *70*, 243−253.

(17) Digdaya, I. A.; Sullivan, I.; Lin, M.; Han, L.; Cheng, W.-H.; Atwater, H. A.; Xiang, C. A Direct Coupled Electrochemical System for Capture and Conversion of CO_2 from Oceanwater. *Nat. Commun.* **2020**, *11*, 4412.

(18) Schiffer, Z. J.; Lucas, É.; Watkins, N. B.; Ardo, S.; Xiang, C.; Atwater, H. A. Acid and Base Generation via an Electrochemical Hydrogen-Looping Cell Tailored for Carbon Removal Applications. *Device* **2024**, *2*, 100506.

(19) Bustillos, S.; Prentice, D.; La Plante, E. C.; Wang, B.; Sant, G.; Simonetti, D. Process Simulations Reveal the Carbon Dioxide Removal Potential of a Process That Mineralizes Industrial Waste Streams via an Ion Exchange-Based Regenerable pH Swing. *ACS Sustainable Chem. Eng.* **2022**, *10*, 6255−6264.

(20) Lammers, L. N.; Duan, Y.; Anaya, L.; Koishi, A.; Lopez, R.; Delima, R.; Jassby, D.; Sedlak, D. L. Electrolytic Sulfuric Acid Production with Carbon Mineralization for Permanent Carbon Dioxide Removal. *ACS Sustainable Chem. Eng.* **2023**, *11*, 4800−4812.

(21) Ellis, L. D.; Badel, A. F.; Chiang, M. L.; Park, R. J.-Y.; Chiang, Y.-M. Toward Electrochemical Synthesis of Cement—An Electrolyzer-Based Process for Decarbonating CaCO3 While Producing Useful Gas Streams. *Proc. Natl. Acad. Sci. U. S. A.* **2020**, *117*, 12584−12591.

(22) Miao, R. K.; et al. Electrified Cement Production via Anion-Mediated Electrochemical Calcium Extraction. *ACS Energy Lett.* **2023**, *8*, 4694−4701.

(23) Leão, A.; et al. ZeroCAL: Eliminating Carbon Dioxide Emissions from Limestone's Decomposition to Decarbonize Cement Production. *ACS Sustainable Chem. Eng.* **2024**, *12*, 15762−15787.

(24) Zhang, Z.; Williams, A. S. R.; Ren, S.; Mowbray, B. A. W.; Parkyn, C. T. E.; Kim, Y.; Ji, T.; Berlinguette, C. P. Electrolytic Cement Clinker Precursor Production Sustained through Orthogonalization of Ion Vectors. *Energy Environ. Sci.* **2025**, *18*, 2395−2404.

(25) Cassaro, C.; Virruso, G.; Culcasi, A.; Cipollina, A.; Tamburini, A.; Micale, G. Electrodialysis with Bipolar Membranes for the Sustainable Production of Chemicals from Seawater Brines at Pilot Plant Scale. *ACS Sustainable Chem. Eng.* **2023**, *11*, 2989−3000.

(26) Tian, W.; Wang, X.; Fan, C.; Cui, Z. Optimal Treatment of Hypersaline Industrial Wastewater via Bipolar Membrane Electrodialysis. *ACS Sustainable Chem. Eng.* **2019**, *7*, 12358−12368.

(27) Reig, M.; Casas, S.; Valderrama, C.; Gibert, O.; Cortina, J. Integration of Monopolar and Bipolar Electrodialysis for Valorization of Seawater Reverse Osmosis Desalination Brines: Production of Strong Acid and Base. *Desalination* **2016**, *398*, 87−97.
(28) Strathmann, H. Ion-Exchange Membrane Separation Processes. *Membrane Science and Technology Series*, 1st ed.; Elsevier: Amsterdam; Boston, 2004; Vol. *9*.
(29) Mikhaylin, S.; Bazinet, L. Fouling on Ion-Exchange Membranes: Classification, Characterization and Strategies of Prevention and Control. *Adv. Colloid Interface Sci.* **2016**, *229*, 34−56.
(30) Liu, H.; She, Q. Scaling-Enhanced Scaling during Electrodialysis Desalination. *ACS EST Eng.* **2024**, *4*, 1063−1072.
(31) Oener, S. Z.; Twight, L. P.; Lindquist, G. A.; Boettcher, S. W. Thin Cation-Exchange Layers Enable High-Current-Density Bipolar Membrane Electrolyzers via Improved Water Transport. *ACS Energy Lett.* **2021**, *6*, 1−8.
(32) Powers, D.; Mondal, A. N.; Yang, Z.; Wycisk, R.; Kreidler, E.; Pintauro, P. N. Freestanding Bipolar Membranes with an Electrospun Junction for High Current Density Water Splitting. *ACS Appl. Mater. Interfaces* **2022**, *14*, 36092−36104.
(33) Kao, Y.-L.; Buchauer, F.; Serhiichuk, D.; Boettcher, S. W.; Aili, D. Bipolar Membranes Via Divergent Synthesis: On the Interplay between Ion Exchange Capacity and Water Dissociation Catalysis. *ACS Appl. Mater. Interfaces* **2024**, *16*, 58637−58647.
(34) Sasmal, S.; Chen, L.; Sarma, P. V.; Vulpin, O. T.; Simons, C. R.; Wells, K. M.; Spontak, R. J.; Boettcher, S. W. Materials Descriptors for Advanced Water Dissociation Catalysts in Bipolar Membranes. *Nat. Mater.* **2024**, *23*, 1421−1427.
(35) Han, S.; Sasmal, S.; Shen, M.; Wu, Y.; Vulpin, O. T.; Hou, S.; Kim, S.; Lee, J. Y.; Yoon, J.; Boettcher, S. W. Advancing SnO2-Based Water Dissociation Catalysis in Bipolar-Membrane Water Electrolyzers. *ACS Energy Lett.* **2025**, *10*, 1633−1641.
(36) Lucas, É.; Bui, J. C.; Stovall, T. N.; Hwang, M.; Wang, K.; Dunn, E. R.; Spickermann, E.; Shiau, L.; Kusoglu, A.; Weber, A. Z.; Bell, A. T.; Ardo, S.; Atwater, H. A.; Xiang, C. Asymmetric Bipolar Membrane for High Current Density Electrodialysis Operation with Exceptional Stability. *ACS Energy Lett.* **2024**, *9*, 5596−5605.
(37) Vulpin, O. T.; Mitchell, J. B.; Chen, L.; Lim, J.; Sasmal, S.; Price, N. G.; Jarvis, S. R.; Boettcher, S. W. Comparing Advanced Bipolar Membranes for High-Current Electrodialysis and Membrane Electrolysis. *ACS Energy Lett.* **2025**, *10*, 845−852.
(38) Jaroszek, H.; Mikołajczak, W.; Nowak, M.; Pisarska, B. Comparison of the Applicability of Selected Anion-Exchange Membranes for Production of Sulfuric Acid by Electro-Electrodialysis. *Desalination and Water Treatment* **2017**, *64*, 223−227.
(39) Yu, S.; Qian, H.; Liao, J.; Dong, J.; Yu, L.; Liu, C.; Shen, J. Proton Blockage PVDF-co-HFP-based Anion Exchange Membrane for Sulfuric Acid Recovery in Electrodialysis. *J. Membr. Sci.* **2022**, *653*, 120510.
(40) Charnay, B.; Chen, Y.; Misleh, J.; Wright, J. G.; Agarwal, R.; Sauve, E.; Toh, W. L.; Surendranath, Y.; Kanan, M. Membrane-Free Electrochemical Production of Acid and Base Solutions Capable of Processing Ultramafic Rocks. *Nat. Commun.* **2025**, DOI: 10.1038/s41467-025-64595-5.
(41) Mehdizadeh, S.; Yasukawa, M.; Abo, T.; Kakihana, Y.; Higa, M. Effect of Spacer Geometry on Membrane and Solution Compartment Resistances in Reverse Electrodialysis. *J. Membr. Sci.* **2019**, *572*, 271−280.
(42) Weast, R. C. *CRC Handbook of Chemistry and Physics*, 55th ed.; CRC Press, 1974.
(43) Bharmoria, P.; Gehlot, P. S.; Gupta, H.; Kumar, A. Temperature-Dependent Solubility Transition of Na2SO4 in Water and the Effect of NaCl Therein: Solution Structures and Salt Water Dynamics. *J. Phys. Chem. B* **2014**, *118*, 12734−12742.
(44) Davis, J. R.; Chen, Y.; Baygents, J. C.; Farrell, J. Production of Acids and Bases for Ion Exchange Regeneration from Dilute Salt Solutions Using Bipolar Membrane Electrodialysis. *ACS Sustainable Chem. Eng.* **2015**, *3*, 2337−2342.
(45) Gurreri, L.; Tamburini, A.; Cipollina, A.; Micale, G.; Ciofalo, M. Pressure Drop at Low Reynolds Numbers in Woven-Spacer-Filled Channels for Membrane Processes: CFD Prediction and Experimental Validation. *Desalination and Water Treatment* **2017**, *61*, 170−182.
(46) Cerva, M. L.; Liberto, M. D.; Gurreri, L.; Tamburini, A.; Cipollina, A.; Micale, G.; Ciofalo, M. Coupling CFD with a One-Dimensional Model to Predict the Performance of Reverse Electrodialysis Stacks. *J. Membr. Sci.* **2017**, *541*, 595−610.
(47) Campione, A.; Gurreri, L.; Ciofalo, M.; Micale, G.; Tamburini, A.; Cipollina, A. Electrodialysis for Water Desalination: A Critical Assessment of Recent Developments on Process Fundamentals, Models and Applications. *Desalination* **2018**, *434*, 121−160.
(48) Wright, J. G.; Charnay, B. P.; Rabinowitz, J. A.; Mariano, R. G.; Kanan, M. W. Rapid Prototyping of Lab-Scale Electrolysis Cells Using Stereolithography and Electroless Plating. *Device* **2023**, *1*, 100049.

https://doi.org/10.1021/acsenergylett.5c02318
ACS Energy Lett. 2025, 10, 5328−5335